

Spectropolarimetry and nebular geometry of the symbiotic star HBV 475^{*}

H. Schild¹ and H.M. Schmid^{1,2}

¹ Institut für Astronomie, ETH-Zentrum, CH-8092 Zürich, Switzerland

² Landessternwarte Heidelberg-Königstuhl, D-69117 Heidelberg, Germany

Received 2 December 1996 / Accepted 13 February 1997

Abstract. We present and discuss spectropolarimetry of the Raman scattered emission features at $\lambda 6825$ and $\lambda 7082$ of the symbiotic nova HBV 475. Meaningful interpretation in relation to the orbital phase requires an improved ephemeris and we first review available photometry and deduce a new period of 956.5 d and minimum epoch at JD 2 444 890.

The flux of the $\lambda 6825$ line varies with photometric phase by about a factor 2.5. The profile normally is triple-peaked with the blue component showing the largest orbital amplitude.

The polarization in the Raman lines depends strongly on the wavelength. At quadrature, it is about 19 % and 10 % in the blue and red line wings of $\lambda 6825$ respectively with polarization angles perpendicular to each other. The percentage polarization in all parts of the profile exhibits phase-locked variations with highest values at quadrature and values close to zero at conjunction. The polarization angle shows hardly any rotation as expected for eclipsing systems. The inclination of the system is found to be $i = 86^\circ \pm 2^\circ$ and the position angle of the orbital plane is 11° .

Polarization measurements are sensitive indicators of the symmetries prevailing in a scattering arrangement. In HBV 475, the Raman scattering geometry has an up-down symmetry with respect to the orbital plane. Near conjunction, a weak line polarization perpendicular to the orbital plane indicates that the scattering geometry is not rotationally symmetric with respect to the binary axis. The observations are compatible with a spherically expanding wind from the cool giant which has a density enhancement in the orbital plane.

We have retrieved an HST image of HBV 475 from the archive which shows extended [O III] $\lambda 5007$ emission. The main nebulosity is aligned with the orbital plane and has a size of $\sim 0.4''$.

Send offprint requests to: hschild@astro.phys.ethz.ch

^{*} Based on observations obtained with the William Herschel and the Isaac Newton Telescope of the Royal Greenwich Observatory, La Palma, Canary Islands, the 1.93m Telescope of the Observatoire de Haute-Provence, France and HST images retrieved from the data archive.

Key words: binaries: symbiotic – binaries: eclipsing – circumstellar matter – scattering – polarization – stars: individual: HBV 475

1. Introduction

Unnoticed by terrestrial observers, HBV 475's career as a symbiotic star began in 1964 when it brightened within a few months by 2.5 magnitudes. It was only several years later that Kohoutek (1969) discovered the unusual object on objective prism plates. Before the outburst, HBV 475 was an inconspicuous variable star of about 15th magnitude (Stienon et al. 1974). Post-outburst spectroscopy showed many strong and variable emission lines and it was soon realized that the object should be classified as a symbiotic star. At that time, this meant little more than a condensed description of the optical spectrum which consisted of strong nebular emission lines superposed on a stellar red giant spectrum. What constituted such objects was largely unknown and the strange spectral behaviour of HBV 475 spawned interestingly divergent scenarios. Some of the more exotic models testified for the creativity of model makers which easily compensated for lacking or poorly calibrated low resolution spectral data.

Already very early models invoked a binary system with an M star and a hot companion which undergoes nova-like outbursts (Dean & Van Citters 1970; Mammano & Righini 1973). Others involved a Wolf-Rayet star exciting a planetary nebula (Crampton et al. 1970) or accompanied by a late type star (Andrillat & Houziaux 1976). Single star models suggesting that HBV 475 was forming a Planetary Nebula were also put forward (Tamura 1977, 1981). Other propositions involved a massive binary with ejected polar caps and an equatorial ring around the hot component (Grygar et al. 1979) or a nova-like object with recurrent outbursts at intervals of 950 d (Iijima & Mammano 1981). The unavoidable Roche-lobe geometry with disk accretion onto the hot component was also thought to be sufficiently realistic (Chochol & Vittone 1986).

A few of the ingredients of these models are still thought to be essential for symbiotic stars. The present day interpretation (of at least these authors) of HBV 475 is of a symbiotic star of the 'slow nova' variety: An M giant is orbited by a white dwarf which ionizes part of the red giant wind (Nussbaumer & Schmutz 1983; Nussbaumer et al. 1986). The white dwarf accreted material from the cool giant's wind. The 1964 outbreak was due to a thermonuclear outburst on the WD surface. The hot component stayed at a high luminosity for two decades and appears to slowly decline now towards its pre-outburst state (Baratta & Viotti 1990; Mürset & Nussbaumer 1994).

In spite of this broad, generally accepted outline of the overall properties of the HBV 475 system, there are few observational facts. Photometry from pre-outburst photographic plates show periodic eclipses. Radial velocity variations were only measured for nebular emission lines and invariably lead to high mass functions of at least a few solar masses (e.g. Grygar et al. 1979; Iijima et al. 1981). The nebular lines are unlikely to reflect solely the orbital motion and the masses of the stellar components and the binary configuration remain still unconstrained.

In order to investigate the HBV 475 system in more detail, we have carried out spectropolarimetric observations of the broad emission lines at 6825 and 7082 Å. These lines are due to Raman scattering of O VI $\lambda\lambda$ 1032,1038 photons via neutral hydrogen (Schmid 1989). Polarization, induced by an asymmetric scattering geometry, has already been observed in a number of symbiotic systems (Schmid & Schild 1994; Harries & Howarth 1996b) and numerical simulations for various scattering regimes have been generated (Schmid 1996; Harries & Howarth 1997). Recorded time sequences of the changing polarization signal potentially allow to determine the orbital configuration and nebular matter distribution in the inner binary environment. Complementary information of symbiotic nebulae at larger scales can be provided by imaging with high spatial resolution. We have retrieved from the HST archive an image of HBV 475 which for the first time shows extended nebular structures.

After describing our new spectroscopic and spectropolarimetric observations, we review in Sect. 3 the available photometry and deduce a new ephemeris. Sect. 4 and 5 deal with the observed intensity and polarization structure of the Raman lines. Polarization variations and their implications for the orbital configuration are discussed in Sect. 6. We then examine the scattering symmetries and the distribution of the neutral material around the red giant and finally present an HST image which shows resolved nebular emission from the HBV 475 system.

2. Observations

An observations summary, listing both, spectropolarimetric and spectroscopic observations, is given in Table 1.

2.1. Spectropolarimetry

HBV 475 was regularly observed with the 4.2m William Herschel Telescope and the ISIS spectrograph/polarimeter. The data were collected by RGO support astronomers as service observa-

Table 1. Summary of observations. Only the 'WHT' observations were polarimetric. Julian dates are respective to 2 440 000. The orbital phase is calculated according to the ephemeris presented in Sect. 3.3. Emission line equivalent widths for the Raman line λ 6825 are given in Å. We include for flux calibrated data the measured line flux.

Date	JD	phase	EW	F*	telescope
1987 Nov 16	7116	2.327	35.0	1.68	INT
1988 Aug 1	7374	2.597	36.4		OHP
1988 Dec 14	7510	2.739	39.2		OHP
1989 Aug 14	7752	2.992	45.0	0.71	OHP
1991 Aug 19	8487.5	3.761	32.6		WHT
1992 Sep 17	8883.4	4.175	43.2		WHT
1992 Oct 6	8901.5	4.194	39.4		WHT
1992 Oct 26	8922.5	4.216	41.8		WHT
1993 Jul 22	9190.6	4.496	35.2		WHT
1993 Aug 23	9222.5	4.530	29.9		WHT
1993 Sep 7	9237.5	4.545	31.0		WHT
1994 Sep 19	9615.4	4.940	36.2		WHT
1994 Oct 22	9648.5	4.975	35.5		WHT

* : in 10^{-12} erg cm $^{-2}$ s $^{-1}$

tions. The first of these observations was described in Schmid & Schild (1994) where the observational details can be found. This first set of observations was taken with the 600R grating and suffered from a degraded spectral resolution because of a focusing error. Subsequent observations were obtained with the 1200R grating which provided a resolution of 0.65 Å. The detector was a coated EEV CCD with 1242×1152 pixels each 22.5 μ m square except for the last observation which was recorded with a TEK CCD of 1024×1024 24 μ m pixels. The wavelength coverage was from 6730 Å to 7190 Å. The slit of 1'' was kept in a fixed direction on the sky and a dekker provided three apertures, one for the object and two for the sky.

A rotatable half-wave plate can be inserted into the beam and each measurement of linear polarization consists of a set of four observations taken at angles of 0°, 22.5°, 45° and 67.5°. A calcite block located below the slit generates two beams with perpendicular polarization. Normally two cycles with exposure times of 10 min in each half-wave setting were obtained. Exposures with the half-wave plate at 0° and 45° yield Stokes Q and the other two yield Stokes U. The details about how the polarization signal was extracted can be found in Schmid & Schild (1994).

A number of polarization standard stars were observed during each night such that instrumental polarization effects could be removed. The instrumental polarization was usually found to be of the order of 0.1%.

2.2. Spectroscopy

We complemented the polarimetric observations with four spectroscopic observations which were used to examine the light curve of the Raman lines. One of these observations was obtained with the Isaac Newton Telescope (2.5m) and the others with the 1.93m telescope of the 'Observatoire de Haute-

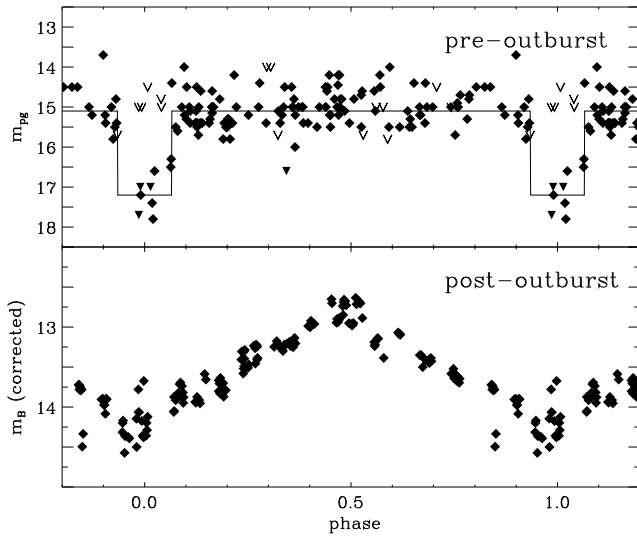


Fig. 1. Pre-outburst and post-outburst light curve phased with the ephemeris $JD_{\min} = 2444890.0 + 956.5 \times E$. Normal data points are plotted as filled diamonds. The upper panel distinguishes between “fainter than” marks with limits $m_{pg} > 16^m$ (filled triangles) and $m_{pg} \leq 16^m$ (∇). The post-outburst data have been corrected for the long term trend.

Provence (OHP)’. A summary of the observing dates and telescopes is given in Tab. 1. The spectrophotometric INT observations were described in Schmid & Schild (1990). The OHP data were gained with the CARELEC spectrograph (Lemaitre et al. 1990) and a RCA CCD ($30 \mu\text{m}$ pixels). Gratings were combined to give a resolution between 3.5 \AA and 12 \AA (FWHM of arc lines). For each run spectra with a wide slit were taken in order to obtain a colour calibrated spectrum. The weather conditions only allowed an absolute calibration for Aug 1989. The photometric accuracy for this and the INT spectrum should reach about 20 %.

3. Orbital period and phase

The investigation of phase locked variations of the polarization signal rests on a well determined ephemeris for the orbital motion. Stienon et al. (1974) presented a light curve from 1890 to 1973 based on the Harvard Plate collection. Their pre-outburst data revealed eclipse like minima with a period of about $P = 959$ days, and post-outburst variations of about 1.5 mag with a similar periodicity. Ephemerides for the light variations in HBV 475 have been re-analyzed in various studies (Grygar et al. 1979; Mueller et al. 1986; Nussbaumer et al. 1986; Munari et al. 1988; Hric et al. 1993). The resulting periods lie between 950 to 975 days and the predictions for the 1994 photometric minimum scatter within a range of 170 days. This uncertainty is too large for our purpose and therefore we re-examine here the photometric variations.

3.1. Pre-outburst light curve

For the pre-outburst light curve we use the 1891–1961 data of Stienon et al. (1974) and Kohoutek & Bossen (1970). Out of the 157 data points, there are ten measurements or limits fainter than 16^m . In our period analysis we search for a periodic time interval within which the system is faint $m_{pg} > 16^m$ and outside of which the system is bright $m_{pg} \leq 16^m$. “Fainter than” marks for data points brighter than 16^m are ignored, because they do not distinguish between the bright and faint states of the system.

The best solution is found for periods $P = 956.3 - 959.8$ d in agreement with Stienon et al. (1974). All measurements except the very first one (upper limit) can be accommodated. This first observation dating from 1891 indicates a low brightness while according to the fit, it lies at phase 0.35 when the system should be bright (Fig. 1). However, before June 1894 only upper limits are reported — perhaps because the system then was truly fainter. Thus we ignore this point. Longer or shorter periods can not avoid the occurrence of bright data points during eclipse phase or further faint data points in the out-of-eclipse phase. The resulting ephemeris of the pre-outburst data is

$$JD_{\min} = 2427687(\pm 20) + 958.0(\pm 1.8) \times E$$

If we allow two measurements (beside the one from 1891) to be in disagreement with the in/out of eclipse phase separation, the allowed period range increases to $P = 953.3 - 960.1$ with also an enlarged uncertainty in the mid-eclipse epoch $T_0 = 2427681(\pm 30)$.

Both, Grygar et al. (1979) and Munari et al. (1988) derive a shorter period from the Stienon et al. (1974) data set. However, their solutions put a bright data point ($m_{pg} = 14.4$) close to mid-eclipse. Note that Munari et al. (1988) have omitted for an unknown reason that point in their phase plot.

3.2. Post-outburst light curve

We use for the post-outburst light curve the data of Arkhipova & Mandel (1973), Arkhipova (1977) and Arkhipova & Ikonnikova (1989). They provide a homogeneous and well sampled data set of UBV photometry from 1971 to 1988. The light curves show, besides the periodic variations, a long term decrease which we compensate by a correction as suggested in Arkhipova & Ikonnikova (1989). Applying sine wave fits to these curves gives for the post-outburst epoch

$$JD_{\min} = 2444866(\pm 25) + 955(\pm 15) \times E$$

The errors are estimated by comparing the least square solutions for the different colours, for data subsets, or for different long term corrections. The derived post-outburst ephemeris is in agreement with Nussbaumer et al. (1986) which is mainly based on IUE line flux variations, and the study of Hric et al. (1993) based on photographic magnitudes. The uncertainties given in the latter work are, however, incredibly small.

3.3. Adopted ephemeris

The pre- and post-outburst light curves give each a well defined minimum epoch, separated by more than 17 000 d. This defines a period of $P = 954.4(\pm 2.5)$ d, if we assume that there is no phase shift between the post-outburst minima and the pre-outburst eclipses. The orbital period is still well determined even if we allow a large phase shift. For example a shift of ± 100 d in the conjunction phase of the post-outburst light curve only leads to an error of ± 6.6 d in the orbital period.

The general agreement in the periods and minimum epochs as derived above, is very good. We believe that the pre-outburst data define a very reliable orbit, because the observations strongly support the interpretation of stellar eclipses in a binary system. The UBV post-outburst light curves, on the other hand, are dominated by nebular emission and therefore may originate in an extended region. Parts of the emission region may also be misaligned with respect to the binary axis, causing a shift between photometric extrema and orbital conjunction phases. The symmetric appearance of the phase diagram (Fig. 1) indicates, however, that such a phase shift is small.

Here we adopt an ephemeris which primarily has no contradictory points in the pre-outburst eclipse light curve and also fulfills the other period and minimum-epoch conditions:

$$JD_{\min} = 2\,444\,890.0 + 956.5 \times E$$

The corresponding phase diagrams for the pre-outburst and B-band post-outburst are shown in Fig. 1. This solution gives for the pre-outburst light curve a duration of the minimum phase of 125 days. The adopted minimum epoch is at the border of the allowed range of the post-outburst ephemeris. Longer periods move the minimum epoch such that a phase shift between orbital conjunction and photometric extrema occurs.

4. Raman line intensity and structure

4.1. Equivalent widths and fluxes

We list the observed $\lambda 6825$ equivalent widths in Table 1. The red giant continuum underlying $\lambda 6825$ is relatively unstructured and the accuracy of the EW's is about 5%.

The $\lambda 6825$ equivalent widths can be converted into approximate line fluxes. Our spectroscopic data show that the observed variations in the UBV filters and at $\lambda 6825$ are mainly due to a changing nebular continuum flux. We measure a constant ratio between the mean V flux in the 5000–6000 Å range F_V and the continuum flux at 6825 according to $F_c(\lambda 6825) = 1.5(\pm 0.1) \cdot F_V$, where $F_V = 3.75 \cdot 10^{-9} \times 10^{(-0.4 \cdot m_V)} \text{ erg cm}^{-2} \text{ s}^{-1} \text{ Å}^{-1}$. For the flux in the V band we use a simple fit of the form $m_V = 13.1 + 0.55 \cdot \cos(2\pi \phi)$ where ϕ is the phase of the adopted ephemeris. Clearly, this indirect calibration of line fluxes involves some uncertainty but the two flux measurements from Nov 1987 and Aug 1989 are in good agreement with our procedure.

Fig. 2 shows the measured $\lambda 6825$ equivalent widths and the corresponding estimated line fluxes as a function of phase. The

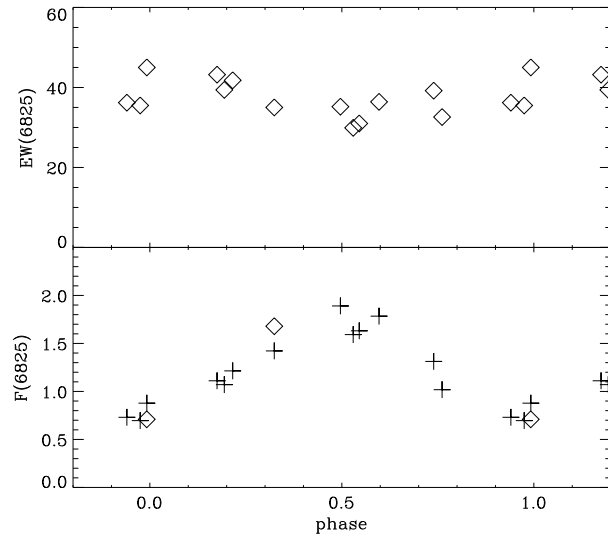


Fig. 2. Equivalent widths in Å (top) and line fluxes in $10^{-12} \text{ erg cm}^{-2} \text{ s}^{-1}$ (bottom) for the $\lambda 6825$ line. Diamonds are measured values and crosses are flux estimates based on conversion of measured EWs via a fit to the V-band photometry (see text).

Raman equivalent widths are rather constant over the orbital period although one may suspect a weak minimum at photometric maximum. The estimated line fluxes show an apparently sine-like variation where the maximum flux is about $2.5(\pm 0.5)$ times the strength of the minimum flux

Equivalent widths $EW(6825)$ for the years 1977–1987 were presented in Arkhipova & Ikonnikova (1989). They measured very similar values although with a larger scatter. This suggests that the cyclic behaviour of the $\lambda 6825$ line flux has been very regular since at least 1977. The estimated line intensities given in Arkhipova & Ikonnikova (1989) show qualitatively the same behaviour as in Fig. 2, but their absolute values are higher by a factor 2. Given the uncertainties in the absolute calibration, there is however no real indication for a long-term systematic trend.

For all, except the Aug 1991 observation, which had a degraded resolution, we have measured a flux ratio $F(\lambda 6825)/F(\lambda 7082)$. The ratio appears to be constant with time, with a mean value of 6.0 ± 0.3 .

4.2. Raman line structure

The Raman $\lambda 6825$ line profiles display a triple-peak structure at all phases. The red peak is always weakest and shows only relatively small variations. The central peak appears to be composed of two unresolved components, the relative contributions of which vary as a function of phase. The blue component is strongest except near eclipse and also displays the strongest variations. Fig. 3 shows the $\lambda 6825$ profiles observed near maximum (Jul 1993) and eclipse (Oct 1994), together with the ratio of these observations. As expected for a circular orbit, the two line profiles are not shifted in wavelength because the motion

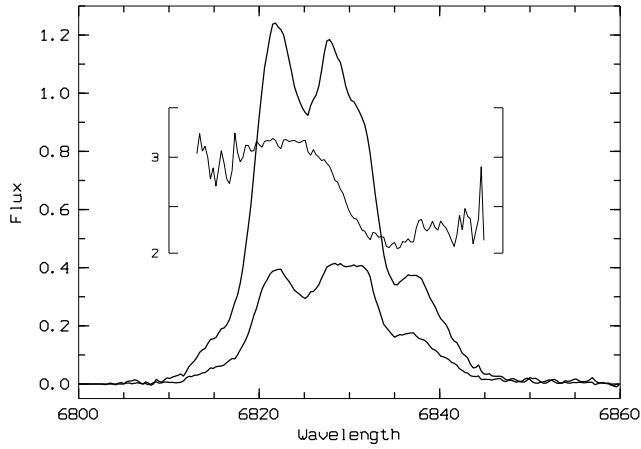


Fig. 3. Raman $\lambda 6825$ line profiles of HBV 475 at maximum and eclipse in units of $10^{-13} \text{ erg cm}^{-2} \text{ s}^{-1} \text{ \AA}^{-1}$. The inset shows the intensity ratio

of the neutral hydrogen scatterers relative to the O VI emission zone is independent of phase. The intensity ratio is a smooth function which does not show the triple-peak structure. It has a high value of about 3 in the blue component and is significantly smaller in the red component. A smooth transition between these values occurs across the central peak.

The $\lambda 7082$ profile is weaker and hence more noisy. It is also additionally structured by underlying stellar molecular absorption bands. We have corrected for these stellar features by subtracting a suitable standard star (BS 8940). The resulting profile differs substantially from the $\lambda 6825$ profile (Fig. 4). It only shows two bumps and the blue peak is always much weaker than the red one. The central depression appears to be deeper at least in those spectra which have sufficient signal.

The occultation ratio (maximum/minimum) is remarkably similar for both Raman profiles. The light attenuation factor in the blue wing of $\lambda 7082$ is ~ 4 which is slightly higher than for $\lambda 6825$ but in the red wing there are no significant differences.

5. Raman line polarization

The observed linear polarization, described by the parameter set (I, Q, U) or (I, p, γ) , consists of the intrinsic polarization (I^0, Q^0, U^0) and the interstellar polarization induced by dust grains. As in Schmid & Schild (1994) we use the indices ℓ and c for the measured line and continuum polarization, respectively. The intrinsic polarization, after correction for the interstellar polarization, is denoted with the indices L and C . We thus have

$$\frac{Q}{I} = \frac{Q_c + Q_\ell}{I_c + I_\ell} \quad (1)$$

$$\frac{Q^0}{I^0} = \frac{Q_C + Q_L}{I_C + I_L} \quad (2)$$

and similarly for Stokes U.

5.1. Interstellar polarization

In all our polarimetric observations we detect a small but measurable continuum polarization. Within the errors, this polarization appears to be constant and summing the data we obtain $Q_c/I_c = 0.77(\pm 0.20)\%$ and $U_c/I_c = 0.76(\pm 0.20)\%$ which is equivalent to a percentage polarization of $p_c = 1.08(\pm 0.28)\%$ at an angle of $\gamma_c = 22(\pm 8)^\circ$. The uncertainties are one-sigma deviations between our 9 measurements and are due to remaining calibration errors and photon noise.

Our measurement closely matches the values of Schulte-Ladbeck (1985) obtained in V, I and $H\alpha$ filters. This continuum polarization is consistent with the interstellar polarization expected to be present in the field of HBV 475 (Schmid & Schild 1994). Also the fact, that the polarization in the $H\alpha$ filter is the same as in the I filter, which is dominated by red giant light, strongly indicates that the polarization is interstellar in origin and not intrinsic to the system (Schulte-Ladbeck 1985). Since the interstellar contribution is small we can, to a good approximation, correct for it with:

$$\frac{Q^0}{I^0} \simeq \frac{Q}{I} - p_c \cos 2\gamma_c \quad (3)$$

$$\frac{U^0}{I^0} \simeq \frac{U}{I} - p_c \sin 2\gamma_c \quad (4)$$

5.2. Intrinsic Raman polarization

We obtain the intrinsic line polarization Q_L/I_L by inserting equation (3) into (2) and analogously for U_L/I_L . Since there is no continuum polarization intrinsic to the symbiotic system $Q_C = U_C = 0$. In the following we use the primed quantities Q' and U' which are Stokes parameters rotated into a system aligned with the intrinsic mean polarization direction. They always refer to intrinsic line polarizations but, for better readability, we drop the index L . In the case of HBV 475, the required rotation is 100° and the same for all observing dates. Stokes Q' is thus at a position angle of 100° (North over East). We list in Table 2 the relative Stokes parameters Q'/I , U'/I integrated over the full $\lambda 6825$ line and in five wavelength bins covering the full $\lambda 6825$ line from 6815 to 6840 \AA . The polarization signal shows strong variations in Q'/I but the U'/I component is very weak.

Our polarimetric data were taken in four consecutive observing seasons. Due to the long orbital period (2.6 years) the observations from the same year correspond to similar orbital phases. We thus have one observation from 1992 near phase 0.75 or second quadrature, three observations from 1992 near phase 0.2 or first quadrature, three observations from 1993 around phase 0.5 (maximum), and two 1994 observations close to phase 1.0 (minimum). The observations in a given yearly group have very similar intensity and polarization profiles. For clarity we show in Fig. 4 the intrinsic Stokes parameters I , Q' , U' and Q'/I of the averaged profiles for 1992 (quadrature), 1993 (maximum), and 1994 (minimum). The individual profiles are also shown as dots such that the intrinsic deviations can be seen. Fluxes and Stokes

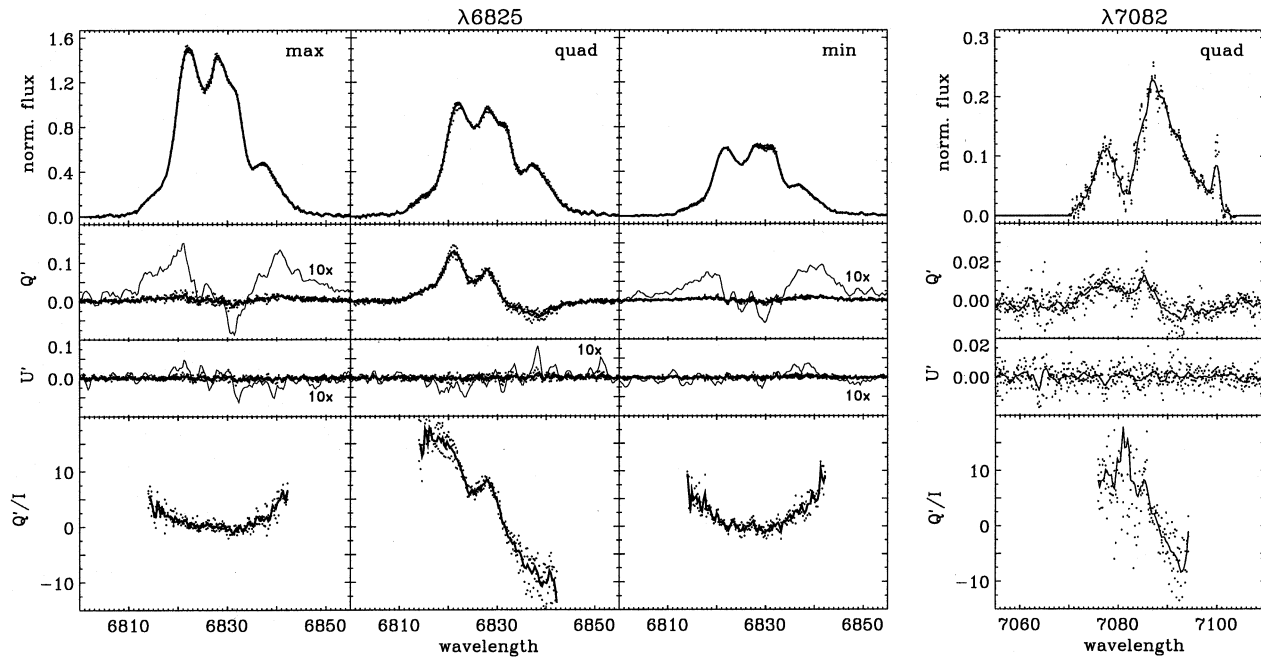


Fig. 4. Polarization spectra of the Raman lines $\lambda 6825$ (left) and $\lambda 7082$ (right) in HBV 475. Individual observations are given as dots. Full lines are means for a group of observations taken at similar phase, near photometric maximum, near quadrature or near minimum. Thin lines are additionally smoothed with a 5 pixel boxcar and in the case of $\lambda 6825$, enlarged by a factor 10. For $\lambda 7082$ only the quadrature observation is given because the polarization signal for maximum and minimum is too small. All data are corrected for the interstellar polarization and the continuum radiation has been subtracted.

Table 2. Polarization in the Raman $\lambda 6825$ line. The polarization is expressed as flux weighted relative Stokes parameters Q'/I and U'/I (percentage) in a rotated coordinate system with the Q' axis at a position angle of 100° . Values are given for the entire line and 5 subintervals corresponding to the extreme blue, blue, middle, red and extreme red portions of the line.

Obs. JD	total		[6815–6820]		[6820–6825]		[6825–6830]		[6830–6835]		[6835–6840]	
	Q'/I	U'/I	Q'/I	U'/I	Q'/I	U'/I	Q'/I	U'/I	Q'/I	U'/I	Q'/I	U'/I
8487.5	4.49	1.14	18.9	0.3	13.1	0.6	7.5	0.9	1.1	1.7	-9.8	1.7
8883.4	4.79	-0.44	13.9	-1.0	9.4	-0.6	6.6	0.2	0.2	-0.7	-6.3	0.0
8901.5	4.77	0.12	16.8	-0.8	10.6	0.0	6.9	0.2	-0.2	0.3	-7.5	-0.4
8922.5	4.13	0.42	16.8	0.0	11.2	-0.2	7.5	-0.4	-1.7	0.5	-11.2	1.9
9190.6	0.63	0.04	1.3	0.4	0.2	0.4	-0.3	0.1	-0.5	-0.2	1.4	-0.1
9222.5	1.39	-0.22	2.1	-0.2	0.7	0.2	0.3	-0.1	-0.2	-0.6	2.6	-0.3
9237.5	1.19	-0.11	2.7	0.4	1.0	-0.3	0.5	0.0	-0.6	0.2	1.2	-1.3
9615.4	0.87	-1.07	2.4	-0.8	0.4	-0.5	-0.9	-0.6	-0.5	-0.1	2.1	-0.5
9648.5	2.05	1.06	3.5	0.5	0.4	0.3	0.3	0.3	0.6	0.4	4.2	3.0

parameters were normalized relative to the $\lambda 6825$ quadrature observation (peak intensities = 1), assuming that for a given group the individual fluxes are equal and adopting the phase dependent line flux variation as described in Sect. 4.1. The data from the second quadrature in 1991 are published in Schmid & Schild (1994). They are very similar to the first quadrature observations from 1992 except for the reduced resolution.

The profiles Q'/I at maximum and minimum are very similar and flatish whereas at quadrature there is a steep decrease

with increasing wavelength. We note that the polarization in this coordinate frame is $p = |Q'/I|$ and the polarization angle $\gamma' \approx 0^\circ$ for $Q'/I > 0$ and $\gamma' \approx 90^\circ$ for $Q'/I < 0$.

Fig. 4 also shows, as an illustration, the intrinsic Stokes parameters of the $\lambda 7082$ line at quadrature. It is evident that, in spite of the different intensity profile, the polarization structure is very similar in both Raman lines.

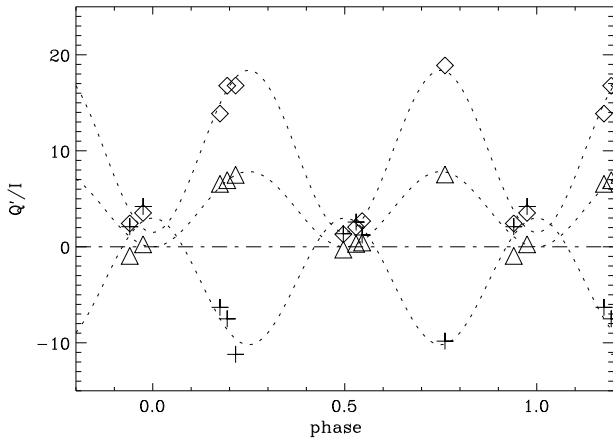


Fig. 5. Phase-dependence of rotated Stokes Q'/I [%] for the extreme blue line wing (diamonds), the line center (triangles), and the extreme red line wing (crosses) of the $\lambda 6825$ feature. The dashed lines represent fits of the form $a \sin^2 \phi + b$

6. Polarization variation and orbit

6.1. General

For an interpretation of the Raman polarization signals we adopt the model scattering geometry described in Schmid & Schild (1994) and Schmid (1996): The O VI radiation is produced in the ionized region near the hot component and converted into Raman photons by neutral hydrogen in the extended and spherically expanding atmosphere of the cool giant. The Raman photons in the blue line wing originate in the neutral region between the two stars. This region is illuminated along the binary axis and the O VI photons are Doppler shifted by approaching H^0 -atoms. The blue shifted Raman photons therefore have a polarization perpendicular to the binary axis. Scatterings by receding H^0 -atoms in the outer wind regions produce the red line wing. From there a polarization parallel to the binary axis is expected if O VI photons propagating away from the binary axes can also be Raman scattered.

6.2. The case of HBV 475

The variations in Q'/I are locked to the orbital phase (Fig. 5). The polarization signals are strongest at quadrature phases. Then the extreme blue and central part of the profile have a positive and the extreme red wing a negative Q'/I polarization. Near conjunction Q'/I is close to zero. The observed phase behaviour can be approximated with a function $Q'/I = a \sin^2 \phi + b$, where a is positive for the blue-middle part and negative for the extreme red wing.

Such a simple $\sin^2 \phi$ -like phase behaviour is very similar to model calculations (e.g. Schmid 1996) for an edge on binary system where the scattering geometry is rotationally symmetric with respect to the binary axis. Rotationally symmetric models do however predict a strict cancelation of the polarization signal at conjunction phases. This seems to happen for the line center where the polarization is, within the measuring uncertainties,

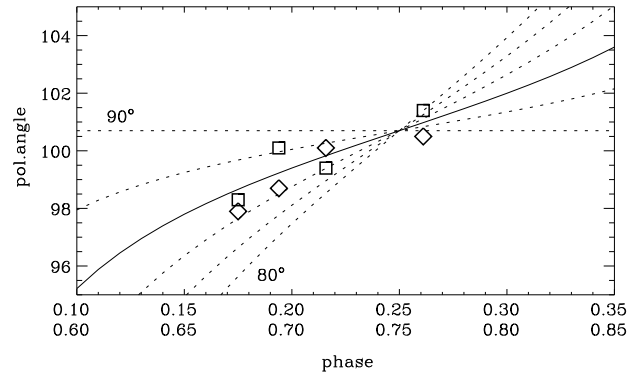


Fig. 6. Polarization angles in the blue portion of the Raman line $\lambda 6825$ for observations near quadrature. Diamonds indicate the angle in the wavelength interval [6815–6820] and squares in [6820–6825]. Dotted lines give fits for the expected angle rotation for orbital inclinations between $i = 80^\circ$ and 90° . The best solution $i = 86^\circ$ is given as full line.

equal to zero. But, both the blue and red line wing show a small but measurable positive polarization in the Q' -direction. This requires a small deviation from rotational symmetry or another effect distorting the scattering geometry (see Sect. 7.2).

6.3. Orientation of the orbital plane

The polarization angle defines the relative orientation between O VI light source and scattering region projected onto the sky. In the model described above, the binary axis is perpendicular to the polarization angle in the blue line wing. We measure near quadrature phases an angle of about 100° . A least square fit procedure, which simultaneously adjusts the orbit orientation and the inclination provides a solution for the orbital position angle of 11° with an average deviation of 0.5° . We thus adopt for the orbital plane of HBV 475 a position angle of $11 \pm 2^\circ$ (North over East). This direction corresponds to the line of nodes for the orbital plane. There exists, as always in polarimetric orbit determinations, an 180° ambiguity in the position angle of the ascending node.

6.4. Inclination

For an orbital inclination of $i = 90^\circ$ the above scattering geometry produces a strong oscillation in the percentage polarization but no changes in the angle. This reflects the fact that the polarization angle is locked to the orientation of the binary axis, which has always the same projected direction.

The observations of HBV 475 are qualitatively very similar to such an $i = 90^\circ$ -model. Around quadrature the polarization is very strong and the polarization angle is dominated by the general orientation of the scattering geometry. At that epoch, a systematic (roughly linear) trend in the polarization angle should be measurable, if the inclination differs from $i = 90^\circ$. Fig. 6 shows the measured polarization angles in the blue line wing for our quadrature observations together with the expected orientations

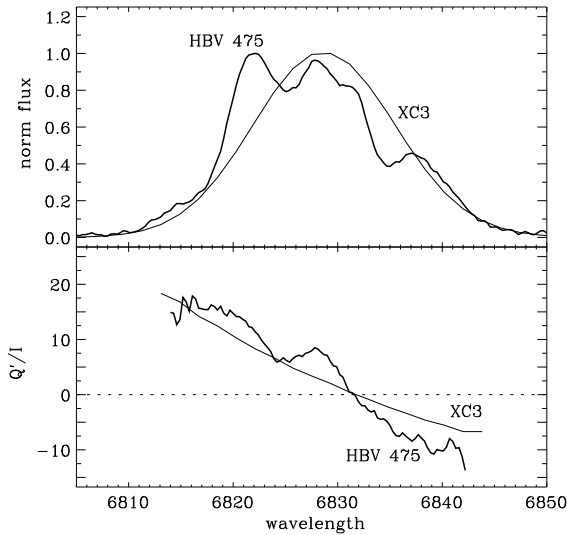


Fig. 7. Spectropolarimetric structure Q'/I of the Raman line $\lambda 6825$ at quadrature phase for HBV 475 and the scattering model XC3.

of circular orbits with different inclinations. We estimate that the accuracy of a single polarization angle measurement is about $\pm 1^\circ$. From Fig. 6 we obtain a best solution for the inclination of $i = 86^\circ \pm 2^\circ$. A least square fitting procedure which simultaneously adjusts the orbit orientation and inclinations provides the same result.

Our estimated error margin only takes the intrinsic scatter into account. From previous polarization studies of SY Mus (Harries & Howarth 1996a) and AG Dra (Schmid & Schild 1997) it is however known that deviations in the polarization angle of a few degrees from a formal orbital fit solutions may occur. Such discrepancies can be caused by time-variable misalignments of the scattering geometry with respect to the binary axis.

7. Scattering geometry

7.1. Comparison between HBV 475 and model XC3

The observed properties of the Raman lines of HBV 475 can be compared with the numerical 2-d simulations of Schmid (1996). A reasonable first order fit of the observations is achieved with the model XC3 (Fig. 7) which has an ionisation parameter $X_{H^+} = 0.4$ corresponding to a cone-shaped ionization region around the hot component. The same symbiotic star model (SC3) is used in Schmid (1995) to simulate the variations of the UV continuum and emission lines due to Rayleigh scattering. The overall agreement as seen in Fig. 7 is encouraging but there are also notable differences particularly in Stokes I. The observed intensity profile is multi-peaked, a feature which was recently reproduced in the models of Harries & Howarth (1997).

Model XC3 produces for the $\lambda 6825$ Raman line at quadrature an integrated polarization of $Q/I = +2.9\%$, a polarization of $Q/I = +17\%$ in the blue line wing at 6815\AA and $Q/I = -5.5\%$ in the red line wing at 6840\AA . This is in very

good agreement with the observations. The phase dependence of the polarization signal is for both, observations and simulations, similar to a $\sin^2\phi$ -function. In addition, the model line ratio of $F(\lambda 6825)/F(\lambda 7082) = 5.3$ is close to the observed value of 6.3 and the Rayleigh scattering model gives for the UV line N v $\lambda 1240$ strong sine-like variations as observed for HBV 475 with IUE (e.g. Nussbaumer et al. 1986).

On the other hand, the model predicts practically phase-independent Raman line fluxes in contrast to the observed flux variations. Model XC3 also produces significant differences in the polarization of the $\lambda 6825$ and $\lambda 7082$ lines, and significant differences in the light curve of various UV lines. Such a behaviour is however not observed, neither in HBV 475, nor in most other symbiotic systems. These discrepancies could be ascribed to an underestimate of the absorption of O VI radiation in the scattering zone as discussed in Schmid (1995, 1996). Another difficulty is the observed non-zero polarization around conjunction, which indicates a non-axisymmetric scattering geometry (see below). Of course, such a 3-dimensional effect is not obtained in the axisymmetric model calculations.

The scattering models depend strongly on the parameter X_{H^+} which describes the geometry of the ionization structure and the mass loss rate \dot{M} of the cool giant. Thus, if we accept the XC3 model scaled with the factor $x = 1.2$ (Schmid 1995) as representative for HBV 475, we estimate a mass loss rate of $\dot{M} = 1.45 \cdot 10^{-6} M_\odot/\text{yr}$ with $v_\infty = 20$ km/s for the cool component. This polarimetric mass loss rate is in general agreement with the rate deduced from radio observations. Seaquist et al. (1993) obtained $\dot{M} = 8.9 \cdot 10^{-7} M_\odot/\text{yr}$ with an adopted expansion velocity $v_\infty = 30$ km/s. The radio mass loss rate is a lower limit because the employed Wright & Barlow (1975) formula assumes full ionization of the wind.

7.2. On the 3-dimensional geometry

Near quadrature the Raman line polarization has two position angles perpendicular to each other. Such a polarization signal is expected from a scattering geometry with a mirror symmetry. The plane of symmetry is identical with the orbital plane. This conclusion is unavoidable for an eclipsing object if the basic scattering model of Sect. 6.1 is adopted. The presence of an up-down symmetry with respect to the binary axis is also from a theoretical viewpoint a simple and attractive configuration.

Near conjunction a non-zero polarization signal remains in the blue and red wings of the $\lambda 6825$ line. During these phases the O VI light source is either in front of the scattering region or behind it. Geometric compensation would strictly nullify the polarization if both, light source and scattering region, are rotationally symmetric relative to the binary axis. The polarization angle in both, the blue and red line wing, is close to 100° . Deviations from this value are always less than 10° and not significant in the blue line wing. In the red line wing we measured 76° for $\text{JD}_{244} = 9237.5$ and 118° for $\text{JD}_{244} = 9648.5$, and an angle compatible with 100° for the other three observations near conjunction. The polarization in the blue and red line wing is roughly at a 90° angle with the orbital plane.

We propose here a modified scenario in which the cool giant is surrounded by a neutral and expanding wind region with an increased density in the equatorial region. Such an equatorial density enhancement is not in conflict with the observed line variations which are symmetric with respect to the nominal eclipse phase.

In a flattened geometry, relatively more O VI photons scatter in the equatorial region. This means that the scattered photons with a polarization perpendicular to the binary plane are more frequent. The induced polarization is smallest for scatterings near the binary axis because this corresponds at conjunction to a back-scattering or forward-scattering situation which produces no polarization. Larger polarizations signals are expected from the outer wind regions where we observe Raman processes with larger scattering angles. As in the case with the spherically symmetric giant wind, the inner region near the binary axis produces a blue shifted Raman photon and the outer region a red shifted one.

Thus, due to the density contrast we expect at conjunction a polarization signal in the Raman line which increases towards the red line wing. Simple estimates suggest that a perpendicular polarization of several percent can be reached if the photons originating from near the hot component have twice the probability of being scattered in the outer equatorial region, than in the outer polar region.

At conjunction, the central part of the Raman line shows no or only little polarization. This depolarization could be due to the fact that a substantial fraction of O VI photons penetrate deeply into the neutral region and reach the outer “quasi-static” atmosphere of the cool giant. This region has a structure which is probably close to a spherical symmetry and geometric compensation nullifies the polarization near conjunction. Scatterings in this region would produce no Doppler shifts and therefore mainly contribute an unpolarized component in the line center. Note that this “quasi-static” region must be larger than the red giant’s photosphere in order to avoid full eclipse of this contributing minimum.

Two effects could account for the polarization in the blue line wing. A perpendicular component would result if the O VI emission originated in an elongated structure in the equatorial plane. The scatterings in the equatorial plane have then on average a larger scattering angle (differ more from a strict back- or forward-scattering) and therefore induce a net perpendicular polarization component. Note however, that the elongated O VI region would also induce a similar (although smaller) net polarization component for scatterings in the spherical atmosphere of the cool giant. The blue wing polarization could also be a multiple scattering effect due to enhanced density in the equatorial region. Rayleigh scattered photons will have a higher probability to escape in the polar direction. Thus Rayleigh scattered photons which propagate along the equatorial plane have the higher probability to undergo subsequently a Raman scattering process which will induce predominantly a polarization perpendicular to the equatorial plane.

The above interpretations of the polarization signal at conjunction are tentative. We believe that an enhanced density in the

outer, equatorial scattering region is a very attractive explanation for the polarization in the red line wing. Numerical simulations are needed for a reliable interpretation of the polarization signal at conjunction, especially for the polarization in the blue wing and the absence of polarization in the line center. Only accurate simulations can disentangle the complex interplay in the inner scattering region between geometric compensation, photon escape probability and multiple scattering effects.

8. HST images and extended nebulosity

With the orbital orientation on the sky determined by polarimetric observations, the question arises whether any extended nebular emission is detectable and if so, how it is arranged with respect to the binary plane. To our knowledge, no extended structures around HBV 475, either in the optical or in the radio have been reported. We therefore interrogated the HST archive and retrieved a series of FOC images of HBV 475. All of them were obtained previous to the COSTAR repair mission. Three images were taken in F96 mode but two of them were unusable because of heavy saturation or because the object was placed too close to the edge of the frame. The remaining image was taken on 23 July 1991 through the F501N filter. Light in this filter is dominated by [O III] λ 5007 emission with additional contributions from He I λ 5016 and [Fe II] λ 5018.

We have constructed a theoretical point spread function and deconvolved the image with a Richardson–Lucy algorithm. The resulting image is shown on a logarithmic scale in Fig. 8. Evidently there is some extended [O III] emission detectable. As an independent check we have also deconvolved the image with an observation of the white dwarf HZ 4 which was taken with the same instrumental set-up. Again the same nebular structure around HBV 475 emerges although with much more noise superposed. We therefore can exclude the possibility that instrumental effects like ghosting are responsible for the observed emission pattern.

The nebulosity appears to consist of a linear structure which is aligned with the orbital plane as derived from our polarization measurements and a further extension stretching East-Southeast. Some of the weak details in the southern extension may be deconvolution artefacts but the northern emission blob is very strong and already well visible in the raw data. Its intensity is about one fifth of the central emission peak from which it is separated by 150 mas. At a distance of 3.4 kpc (Mürset et al. 1991) this corresponds to a projected separation of about 500 AU. If this emission blob is due to the 1964 eruption, it must have travelled with a velocity of at least 90 km/s.

Since much of the nebulosity is aligned with the orbital plane, ionization and hence line intensities are expected to be phase-modulated. The image in Fig. 8 was obtained near quadrature at phase 3.73 and we may speculate that the southern section of the nebulosity was faint because the hot component was shadowed by the red companion. In this scenario, the other quadrature phase is predicted to have increased southern emission.

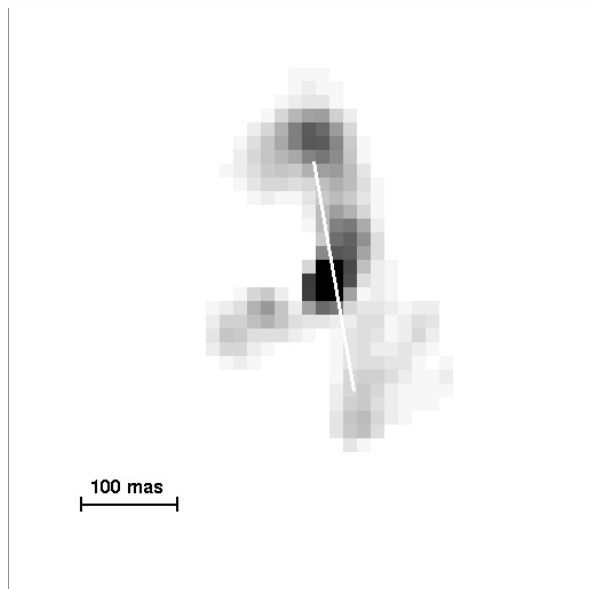


Fig. 8. Deconvolved HST image of HBV 475 in the line of [O III] λ 5007 (filter F501N). The orientation of the orbital plane is indicated by the white line. North is up and East to the left.

High resolution spectroscopic observations have shown phase dependent profile variations in many emission lines. The [O III] λ 5007 profile consists of various emission peaks which change their appearance as a function of orbital phase (Iverson et al. 1994; Tamura 1989). On several occasions emission peaks at velocity displacements of ± 150 to 200 km/s were reported (Wallerstein et al. 1989). The presence of extended circumstellar material is also indicated by absorptions of constant radial velocity in the C IV $\lambda\lambda$ 1548,1551 line profiles (Nussbaumer & Vogel 1991).

9. Discussion

We report detailed results on the polarization structure of the Raman scattered λ 6825 and λ 7082 lines of the symbiotic nova HBV 475. The polarization variations are locked to the orbital phase and the general polarization pattern can be understood in terms of the numerical scattering model of Schmid (1996). The quadrature polarization is qualitatively, and to a large extent also quantitatively, understood. At conjunction phases, polarization deviations from the model predictions occur in the Raman line wings. These discrepancies are probably due to a perturbed rotational symmetry such that scattering material is concentrated towards the binary plane. Such a density enhancement is also theoretically expected because of the combined gravitational pull of the stellar components. Polarization measurements are very sensitive indicators of the presence or absence of symmetries in the distribution of the scattering material. In the case of HBV 475 the neutral material is symmetrically arranged with respect to the orbital plane. We also find from polarimetry as well as HST imaging that the nebular material is concentrated towards this plane.

The polarization also yields information about the orbital system parameters, the most interesting of which are the inclination and orientation on the celestial sphere. In the case of HBV 475, our polarimetry strongly adds to previous evidence that the system is eclipsing. The position angle of the orbital plane is close to North-South. The orbit orientation is an important piece of information if an extended nebular structure is present. In the case of HBV 475 we report the detection of such a nebulosity (Fig. 8). Its size is at least 500 AU and its main body is aligned with the binary plane. The main outflow of material appears to have occurred through the equatorial plane. Interestingly, the matter concentration in the orbital plane found by polarization asymmetries at a small scale (few AU) is reflected and enhanced on a large scale by the nebulosity as seen on the HST image.

Spectropolarimetry of Raman scattered emission lines has already provided interesting clues about the gaseous inter-binary environment in several symbiotics. In the case of the D-type symbiotic V1016 Cyg it was found that the ionization front is probably warped due to the relative wind and orbital motions (Schild & Schmid 1996). For HBV 475 there is a concentration of scattering material towards the orbital plane. Further progress and a quantitative reproduction of the details of the polarization profiles requires more realistic scattering models which allow for 3-d effects.

Acknowledgements. We are indebted to the La Palma support astronomers, particularly René Rutten and Vik Dhillon, who carried out the service observations. We thank Harry Nussbaumer, Urs Mürset and Thomas Dumm for interesting comments on an earlier version of this paper. This work was financially supported by the Swiss National Science Foundation.

References

- Andrillat Y., Houziaux L., 1976, A&A 52, 119
- Arhipova V.P., 1977, Perem. Zvezdy 20, 345
- Arhipova V.P., Ikonnikova N.P., 1989, Sov. Astron. Lett. 15, 60
- Arhipova V.P., Mandel O.E., 1973, IBVS 762
- Baratta G.B., Viotti R., 1990, A&A 229, 104
- Chochol D., Vittone A., 1986, Ap&SS 121, 225
- Crampton D., Grygar J., Kohoutek L., Viotti R., 1970, Astrophys. Letts. 6, 5
- Dean C.A., Van Citters W., 1970, PASP 82, 924
- Grygar J., Hric L., Chochol D., Mammano A., 1979, Bull. Astron. Inst. Czech. 30, 308
- Harries T.J., Howarth I.D., 1996a, A&A 310, 235
- Harries T.J., Howarth I.D., 1996b, A&AS 119, 61
- Harries T.J., Howarth I.D., 1997, A&AS 121, 15
- Hric L., Chochol D., Komzik R., 1993, Ap&SS 201, 107
- Iijima T., Mammano A., 1981, Ap&SS 79, 55
- Iijima T., Mammano A., Margoni R., 1981, Ap&SS 75, 237
- Iverson R.J., Bode M.F., Meaburn J., 1994, A&AS 103, 210
- Kohoutek L., 1969, Inf. Bull. Var. Star No 384
- Kohoutek L., Bossen H., 1970, Astrophys. Lett. 6, 157
- Lemaître G., Kohler D., Lacroix D., Meunier J.P., Vin A., 1990 A&A 228, 546
- Mammano A., Righini M., 1973, Mem. Soc. Astron. Ital. 44, 23
- Mueller B.E.A., Nussbaumer H., Schmutz W., 1986, A&A 154, 313

- Munari U., Margoni R., Mammano A., 1988, *A&A* 202, 83
Mürset U., Nussbaumer H., 1994, *A&A* 282, 586
Mürset U., Nussbaumer H., Schmid H.M., Vogel M., 1991, *A&A* 248, 458
Nussbaumer H., Schmutz W., 1983, *A&A* 126, 59
Nussbaumer H., Schmutz W., Vogel M., 1986, *A&A* 169, 154
Nussbaumer H., Vogel M., 1991, *A&A* 248, 81
Seaquist E.R., Krogulec M., Taylor A.R., 1993, *ApJ* 410, 260
Schild H., Schmid H.M., 1996, *A&A* 310, 211
Schmid H.M., 1989, *A&A* 211, L31
Schmid H.M., 1995, *MNRAS* 275, 227
Schmid H.M., 1996, *MNRAS* 282, 511
Schmid H.M., Schild H., 1990, *MNRAS* 246, 84
Schmid H.M., Schild H., 1994, *A&A* 281, 145
Schmid H.M., Schild H., 1997, *A&A* in press
Schulte-Ladbeck R., 1985, *A&A* 142, 333
Stienon F.M., Chartrand M.R., Shao C.Y., 1974, *AJ* 79, 47
Tamura S., 1977 *Astrophys. Letts.* 19, 57
Tamura S., 1981, *PASJ* 33, 701
Tamura S., 1989, *PASP* 101, 250
Wallerstein G., Solf J., Mikolajewska J., Crampton D., Brugel E., 1989 *PASP* 101, 189
Wright A.E., Barlow M.J., 1975, *MNRAS* 170, 41